Bulletin of the Seismological Society of America, Vol. 100, No. 3, pp. 1241–1251, June 2010, doi: 10.1785/0120090263

Effects of 3D Attenuation on Seismic Wave Amplitude and Phase Measurements

by Brian Savage, Dimitri Komatitsch, and Jeroen Tromp

Abstract We incorporate 3D anelastic attenuation into the spectral-element method for seismic wave propagation. This advancement accommodates lateral variations in anelasticity on global, regional, or local scales. We use the method to investigate the effects of anelasticity in an upper mantle attenuation model in conjunction with a global wave-speed model and in a regional subduction zone model. These investigations reveal substantial and competing amplitude anomalies due to elastic and anelastic variations, but rather minor anelastic effects on the travel times of seismic waves. Seismic studies utilizing amplitude data must therefore consider elastic and anelastic heterogeneity in tandem to avoid mapping one type of heterogeneity into the other.

Introduction

The anelastic structure of Earth holds the key to understanding geologic materials and tectonic processes across a broad range of scales. Unfortunately, due to the complexity of measuring the effects of anelastic attenuation, the number of regional or global anelastic models of the Earth's interior is far smaller than the number of elastic wave-speed models. While tomographic images of Earth's wave speed have greatly improved our understanding of global tectonics, they have also generated a new set of questions, including: (1) what is the laterally varying temperature structure of the mantle, (2) what is the percentage of volatiles and melt in the mantle, (3) where are volatiles and melt present, and (4) how does the Earth vary in chemical composition? Anelastic models of the Earth provide some of the constraints required to answer these questions.

Anelastic structure is controlled to a large extent by temperature and varies differently with composition than elastic structure. It has been suggested that the anelasticity of the Earth can be used as a proxy for temperature (Romanowicz, 1994; Gribb and Cooper, 1998), thus helping to constrain dynamic mantle convection simulations. Combining elastic and anelastic structural information also helps to separate and quantify the competing effects of composition and temperature (Karato, 1993).

On a regional scale, imaging anelastic structure can aid in the discrimination of volatiles from melt. Regional scale problems also benefit greatly from isolating relative influences of composition and temperature. Specifically, partial melt and volatiles exhibit different seismic attenuation effects: small amounts of partial melt, $<5\%$, have very little influence on seismic attenuation (Gribb and Cooper, 2000), while volatiles, such as water and CO_2 (Wiens and Smith, 2003) and larger amounts of partial melt (Jackson *et al.*, 2004), have a considerable impact.

Unfortunately, the construction of an anelastic Earth model is difficult because generating an anelastic model generally involves either comparing amplitudes of observed and synthetic arrivals of surface waves (Selby and Woodhouse, 2002; Gung and Romanowicz, 2004; Dalton and Ekström, 2006) or determining t^*, the integrated value of $1/Q$ (Shearer, 1999), through measurement of the spectral amplitude against frequency for a set of seismic body waves (Bhattacharyya *et al.*, 1996; Warren and Shearer, 2000, 2002). The difficulty lies in making accurate and robust measurements that are indicative of attenuation. Amplitudes of seismic waveforms are easily affected by the characteristics of the earthquake source and, more importantly, by elastic heterogeneity, as will be shown later. Complex wave-speed features impede anelastic imaging at high frequencies due to strong focusing and defocusing effects (Ritsema *et al.*, 2002; Zhou, 2009). The generation of an anelastic model free from elastic contamination requires a reasonably accurate wave-speed model to account for wave-speed-induced amplitude variations. Conversely, efforts to generate a wave-speed model free from anelastic effects suffer from amplitude-phase cross-contamination, but to a lesser extent.

A general anelastic Earth model can be tested through the comparison of observed and synthetic seismograms. Structural models specified in terms of temperature, partial melt, volatile content, and composition may also be tested by translating them into seismic models, that is, wave speeds, density, and attenuation (Hammond and Humphreys, 2000a, b; Hacker and Abers, 2004; Boyd *et al.*, 2004). A forward modeling approach allows direct comparison and evaluation of the competing effects of elastic and anelastic structures, or of variations in partial melt, volatile content, and composition. In the following sections, we present a numerical implementation of 3D anelastic attenuation and demonstrate its use in a

regional subduction zone setting and in the context of global surface waves. Each experiment is designed to highlight the versatility of the method for a range of periods from body to surface waves, and to examine the effects and magnitude of phase and amplitude perturbations due to velocity-only and anelastic-attenuation-only 3D variations.

Constant-Q Absorption-Band Model

We have incorporated 3D anelastic attenuation into the spectral-element method (SEM) for seismic wave propagation on regional and global scales (Komatitsch and Tromp, 1999, 2002a,b). We use the SEM because it provides a number of advantages, including the capability to handle any linear constitutive relation and accurate, free-surface boundary conditions (Chaljub *et al.*, 2007).

In seismology, attenuation (Nowick and Berry, 1972; Aki and Richards, 1980; Dahlen and Tromp, 1998) is observed to be relatively constant over a broad frequency range. This type of constant Q behavior may be approximated by a Maxwell absorption-band solid, which may be constructed by combining N standard linear solids (SLSs) in parallel (Liu *et al.*, 1976; Kanamori and Anderson, 1977; Emmerich and Korn, 1987; Carcione *et al.*, 1988; Carcione, 2007; Moczo *et al.*, 2007). Simple Maxwell or Kelvin-Voigt solids are insufficient, because they do not capture creeping or stress relaxation of the system. Our formulation uses a set of N parallel SLSs, that is, a spring in parallel with a Maxwell solid (Fig. 1), also termed a Zener solid. An alternative approach, used by Emmerich and Korn (1987), involves a set of N Maxwell solids in parallel with a single spring. Moczo and Kristek (2005) and Moczo *et al.* (2007) described both approaches and proved that they are mathematically equivalent. In our formulation based upon a set of SLSs, each solid (Fig. 1) is characterized by of a set of stress and strain relaxation times, which approximate internal friction (attenuation) and a corresponding change in phase (physical dispersion). Combination of these SLSs provides a straightforward method for extending anelastic behavior over a broad period range at the expense of a heavier computational load.

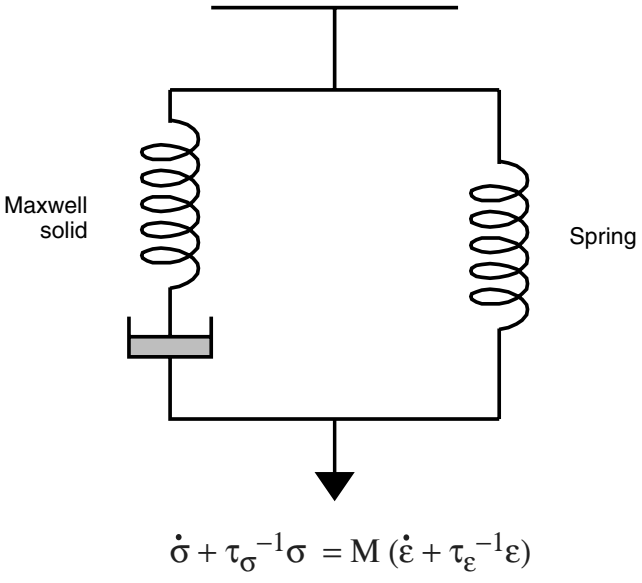

Figure 1. Conceptual model of a standard linear solid (SLS). A spring is combined in parallel with a Maxwell solid. We use a series of standard linear solids to simulate anelasticity, for example, based upon a constant-Q absorption-band model. See Dahlen and Tromp (1998) for a more detailed description of this system.

Within the spectral-element mesh, the SLSs are defined by a period range and an inverse quality factor, $1/Q$, at each numerical integration point. At the start of a simulation, the parameters that characterize the absorption band are computed and stored once and for all, as they are independent of time. Seismic wave speeds are adjusted to accommodate the corresponding physical dispersion.

Period Range

A spectral-element simulation is characterized by a minimum period $T_{\min}$, which is defined by the grid resolution and the minimum wave speed $v_{\min}$:

$$T_{\min} = \frac{\lambda_{\min}}{v_{\min}} = \frac{W N_{\text{points}/\lambda_{\min}}}{v_{\min} N_{\text{GLL}} N_e}, \tag{1}$$

where N_{GLL} denotes the number of Gauss-Lobatto-Legendre (GLL) quadrature points; N_e, the average number of spectral elements along a distance W; and $N_{\text{points}/\lambda_{\min}}$, the number of GLL points per minimum wavelength, $\lambda_{\min}$, which is nominally set equal to approximately 5. Given a minimum wave speed, the time step can be computed in a similar fashion (see De Basabe and Sen, 2007 and Seriani and Oliveira, 2008).

Given the minimum period, $T_{\min}$, absorption-band behavior is mimicked by combining a number of SLSs in parallel to produce a constant quality factor over a desired frequency range. Three SLSs are usually sufficient (Emmerich and Korn, 1987) because they provide a wide enough range to cover approximately 1.7 decades in period with a reasonable degree of accuracy, for example, a period range from approximately 17 sec to 850 sec. Figure 2 shows frequency ranges for various numbers of SLSs where the misfit between the desired internal friction and that represented by the SLSs, between the maximum and minimum frequencies, is minimized. The maximum period is defined as $T_{\max} = T_{\min} \times 10^N$, where N is the number of decades of period for a given number of SLSs. Figure 2 illustrates how well a constant Q model is approximated by increasing numbers of SLSs. A large number of SLSs results in a broader absorption band at a significantly larger computational cost. For three SLSs and an ~1% least-squares error, the optimal absorption-band width covers about 1.7 decades in period. Using a target least-squares error of 1% provides a sufficient period coverage while adequately reproducing the desired absorption band.

Relaxation Times

Once the desired frequency range is established, we need to assign stress and strain relaxation times, τ_{σ_i} and τ_{ϵ_i},

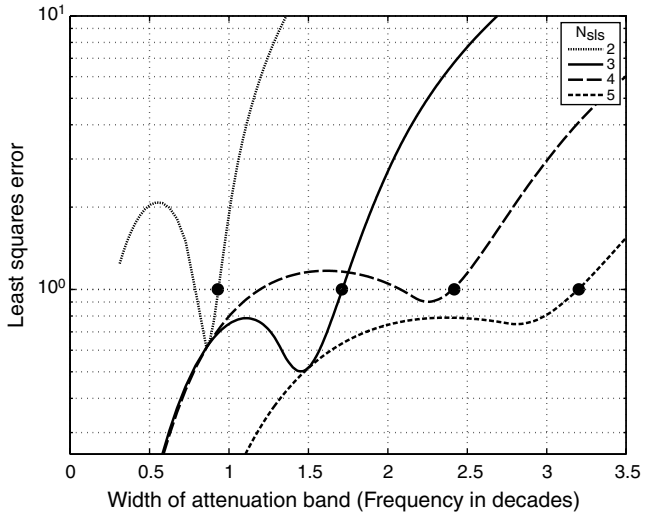

Figure 2. Width of the constant-Q absorption-band with a varying number of standard linear solids, N_{sls}. Each curve represents a different value of N_{sls}, ranging from 2 to 5, plotted against the least-squares error compared with a constant quality factor of $Q = 80$. The total width of the absorption band is indicated for each N_{sls} by the dot at a ~1% least-squares error.

$i = 1, \ldots, N$, respectively. The stress relaxation stress times τ_{σ_i} are chosen independently of the desired quality factor, and are logarithmically spaced evenly along the selected frequency range. Given the desired constant inverse quality factor, $1/Q$, we solve a small optimization problem, typically a linear inversion, to determine the strain relaxation times τ_{ϵ_i}. These stress and strain relaxation times characterize the desired local attenuation, as illustrated in Figure 3.

Following the formulation of Liu *et al.* (1976), we write the general relationship between stress σ and strain ϵ as

$$\sigma = \int_{-\infty}^{t} M(t-\tau)\dot{\epsilon}(\tau)\mathrm{d}\tau. \tag{2}$$

The complex modulus

$$M(t) = M_1(t) + iM_2(t), \tag{3}$$

is used to define the inverse quality factor

$$1/Q = \frac{M_1}{M_2}. \tag{4}$$

A set of N SLSs with stress and strain relaxation times τ_{σ_i} and τ_{ϵ_i}, respectively, has a complex modulus determined by (Liu *et al.*, 1976)

$$M_1 = 1 - \sum_{i=1}^{N} \frac{\omega^2 \tau_{\epsilon_i}(\tau_{\epsilon_i} - \tau_{\sigma_i})}{1 + \omega^2 \tau_{\epsilon_i}^2}, \tag{5}$$

$$M_2 = \sum_{i=1}^{N} \frac{\omega(\tau_{\epsilon_i} - \tau_{\sigma_i})}{1 + \omega^2 \tau_{\epsilon_i}^2}, \tag{6}$$

where ω denotes angular frequency. Given the desired quality factor Q and N evenly spaced stress relaxation times τ_{σ_i} covering the frequency range of interest, N strain relaxation times τ_{ϵ_i} may be determined. In a 3D model, this optimization problem needs to be solved once and for all for each quality factor of interest.

For relatively high values of the quality factor Q, determination of the N strain relaxation times τ_{ϵ_i} is straightforward based upon a linear inversion method, for example, singular value decomposition. However, for small values of the quality factor, that is, very strong attenuation ($Q < \sim 25$), the inversion requires a nonlinear methodology due to the presence of local minima. A robust determination of the relaxation times is essential for automatic and accurate computation of synthetic seismograms, specifically for complex 3D anelastic models. For this reason, we use the nonlinear simplex method (Nelder and Mead, 1965) to produce relaxation times over a wide range of quality factors. As already mentioned, we use this approach to produce an absorption-band solid with a constant value of Q over several decades in frequency, but note that our approach may be readily extended and generalized to include a frequency dependent Q.

Determining the strain relaxation times τ_{ϵ_i}, $i = 1, \ldots, N$, for all Q values is computationally intensive but represents only a small portion of the total simulation time, in particular for large, high-resolution meshes, because it is accomplished once and for all before the start of time marching. Nevertheless, to reduce the computational burden, we implement a lookup table or associative array with keys defined by the attenuation value and a desired resolution. We impose a maximum quality factor to reduce computation because very large quality factors, say $Q > 1000$, do not affect the wave field significantly because the simulation is basically elastic.

Physical Dispersion. In an anelastic medium, attenuation is accompanied by physical dispersion, which results in a change in phase velocity. The effects of physical dispersion for a constant-Q absorption-band model are illustrated in Figure 3. The wave speed of seismic waves depends linearly on logarithmic frequency within the absorption band. Given the modulus M_0 at a reference frequency ω_0, the modulus at angular frequency ω is determined by

$$\frac{M(\omega)}{M(\omega_0)} \approx 1 + \frac{2}{\pi Q_\mu} \ln\left(\frac{\omega}{\omega_0}\right). \tag{7}$$

Time Marching

Once the wave speeds within the mesh are set to their relaxed values, the domain is prepared for time advancement. Emmerich and Korn (1987), Carcione *et al.* (1988), and Moczo *et al.* (2007) incorporated numerical time advancement of anelastic properties into time-domain seismic computations. Komatitsch and Tromp (1999) incorporated attenuation into the SEM through a relaxation spectrum

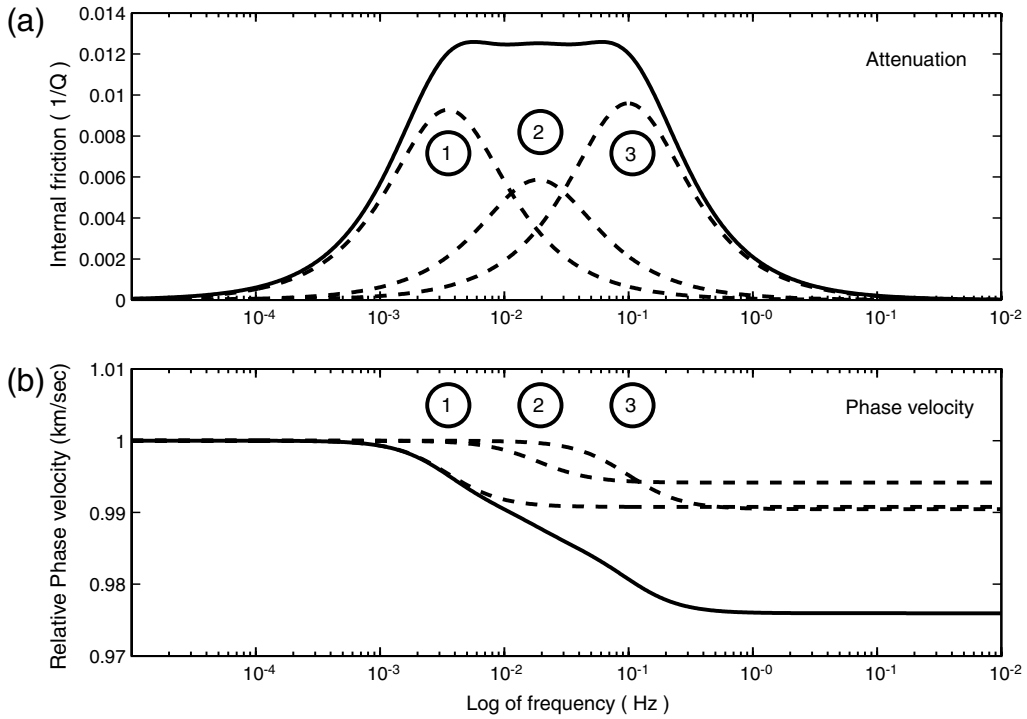

Figure 3. Constant-Q absorption-band model based upon three standard linear solids (Fig. 1). (a) Q^{-1} as a function of logarithmic frequency. The target quality factor is $Q = 80$. Note that Q^{-1} is almost flat as a function of frequency from 3 mHz to 60 mHz, that is, for periods from 16 sec to 330 sec. The individual standard linear solids (numbered 1 to 3 and denoted by the dashed lines) add constructively to create the quasi constant Q absorption-band response. (b) Phase speed as a function of frequency. Note the linear change in phase speed as a function of logarithmic frequency, in accordance with (7). The reference wave speed is scaled to be 1 km/sec.

defined by the set of SLSs discussed previously. Incorporation of the relaxation spectrum modifies the constitutive relationship and the resulting stress by accounting for the time history of the strain.

Time advancement of the relaxation spectrum, and thus attenuation, is accomplished using a fourth order Runge-Kutta integration (Komatitsch and Tromp, 1999), requiring knowledge of the current relaxation spectrum, $R_i(t)$; the stress relaxation times, τ_{σ_i}; the current strain, ϵ; and the previous strains, ϵ'. The scheme is

$$R_i(t+\Delta t) = R_i(t) + \left[\frac{R_i}{\tau_{\sigma_i}} + 2\frac{\Delta M}{\tau_{\sigma_i}}(w'\epsilon' + w\epsilon)\right], \quad (8)$$

$$w'(t) = 1, \quad w'(t+1/2\Delta t) = 1/2; \quad w'(t+\Delta t) = 0, \quad (9)$$

$$w(t) = 0, \quad w(t+1/2\Delta t) = 1/2; \quad w(t+\Delta t) = 1, \quad (10)$$

where ΔM is the difference between the unrelaxed and relaxed moduli. Expansion within the fourth order Runge-Kutta integration results in terms independent of mesh position, strain, time step Δt, and stress relaxation period τ_{σ_i}, which are therefore precomputed. Expansion of the relaxation spectrum derivative, that is, the term in brackets in (8), results in

$$\begin{aligned} R_i(t+\Delta t) = R_i(t) &+ R_i\left(\frac{\Delta t}{\tau_{\sigma_i}} + \frac{\Delta t^2}{2\tau_{\sigma_i}^2} + \frac{\Delta t^3}{6\tau_{\sigma_i}^3} + \frac{\Delta t^4}{24\tau_{\sigma_i}^4}\right) \\ &+ \frac{2\Delta M_i}{\tau_{\sigma_i}}\epsilon'\left(\frac{\Delta t}{2} + \frac{\Delta t^2}{3\tau_{\sigma_i}} + \frac{\Delta t^3}{8\tau_{\sigma_i}^2} + \frac{\Delta t^4}{24\tau_{\sigma_i}^3}\right) \\ &+ \frac{2\Delta M_i}{\tau_{\sigma_i}}\epsilon\left(\frac{\Delta t}{2} + \frac{\Delta t^2}{6\tau_{\sigma_i}} + \frac{\Delta t^3}{24\tau_{\sigma_i}^2}\right). \end{aligned} \quad (11)$$

3D Attenuation Simulations

To test the implementation of anelasticity within the SEM, we investigate the influence of attenuation at short periods for regional arrivals in a subduction zone environment, and then for longer period arrivals of surface waves at the scale of the whole Earth. Implementation of attenuation and other features of the SEM are rigorously tested through a comparison of normal-mode and SEM synthetic seismograms.

Subduction Zone Simulations

We use a model of the Tonga subduction zone consisting of the Zhao *et al.* (1997) 3D tomographic wave-speed model, defined by 3D perturbations on top of the 1D IASP91 wave-speed model (Kennett and Engdahl, 1991), and the attenuation model derived by Roth *et al.* (2000). Roth *et al.* (2000) mapped wave speeds into attenuation through an empirical relationship derived by comparing the Zhao *et al.* (1997) wave-speed model and a 2D tomographic attenuation

model from Roth *et al.* (1999). Perturbations in attenuation were applied to the 1D QM1 attenuation model (Widmer *et al.*, 1991). Synthetic seismograms were calculated for two distinct paths: one traversing the subducting plate, where attenuation is minimal; and a second through the mantle wedge, where substantial attenuation is expected. Cross sections of the wave-speed and attenuation models are shown in Figure 4. The earthquake (12 September 2001 08:48:37:300, UTC) hypocenter is located at 634 km depth.

The effects of 3D wave speed and anelastic attenuation are clearly visible in the synthetic seismograms displayed in Figure 5. Three individual simulations were conducted with different magnitudes of 3D wave-speed variations, including a 1D wave-speed model, a 3D wave-speed model, and a 3D wave-speed model with anomalies at half magnitude. Changes to the synthetic seismograms as a result of wave-speed modifications are displayed in Figure 5, top panel. The synthetics are accurate at periods of approximately 9 sec and longer. When the wave field interacts with the subducting plate included in the 3D tomography model, changes in phase and amplitude are observed for both direct *P* and direct *S* arrivals. With inclusion of faster wave speeds, travel times decrease in tandem with reduced amplitudes. All synthetics at stations near Tonga show a decrease in amplitude and reduction in travel time as the subducting plate is added incrementally, similar to the behavior shown in the top panel

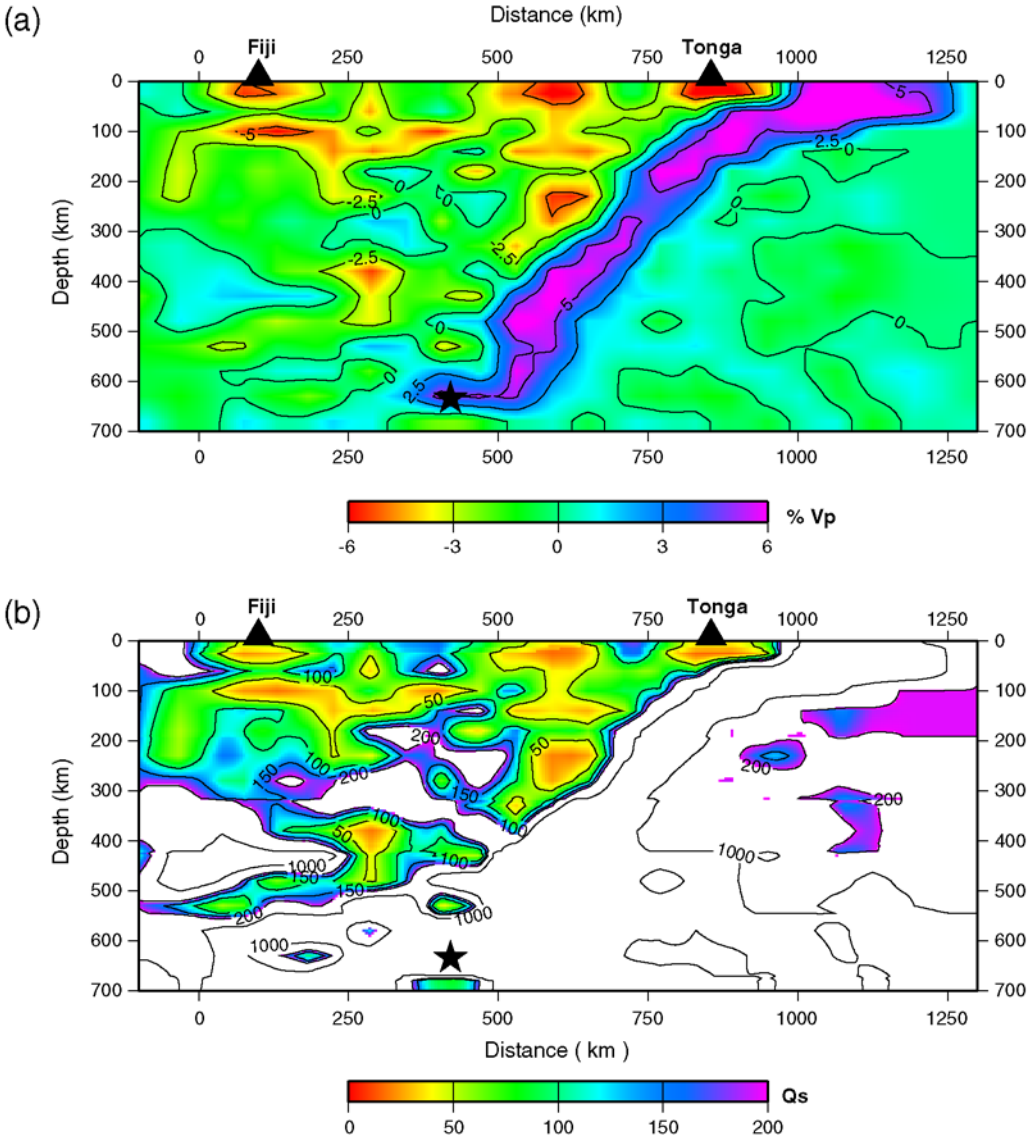

Figure 4. Wave-speed and attenuation models produced by Zhao *et al.* (1997) and Roth *et al.* (2000), respectively, showing the subducting plate near the islands of Tonga and Fiji. (a) The high wave-speed slab is readily identified in the wave-speed image. (b) The attenuation model is based upon an empirical relationship between wave speed and Q (Roth *et al.* 1999). Seismic waves generated by an earthquake represented by the star at 634 km depth are simulated and recorded at seismographic stations in Tonga and Fiji denoted by triangles. Waves traveling to Tonga come up the slab, whereas waves traveling to Fiji traverse the mantle wedge. Very large Q values are displayed as white regions, for example, within the subducting plate. The color version of this figure is available only in the electronic edition.

of Figure 5. Decreased amplitudes in Tonga, for propagation paths along the subducting plate, arise from the faster plate refracting energy or shedding waves away from the interior of the plate (Furumura and Kennett, 2008).

For the same earthquake, a similar but less pronounced change is observed at stations in Fiji when the attenuation model is added (bottom panel of Fig. 5). Recordings of the wave field near the island of Fiji have traversed the mantle wedge, a region of high attenuation. Simulations varying the magnitude of attenuation were conducted to isolate the amplitude and phasing effects. Included in the simulations are a 1D attenuation model, the full 3D attenuation model from Roth *et al.* (2000), and the same attenuation model but with the anomalies doubled in magnitude. The amplitude of the direct S wave is diminished when attenuation is increased from the 1D to the 3D model upon the addition of a low Q mantle wedge. Arrival times of the direct S wave are also affected, but more subtly. This delay of the S wave arrival mimics a small reduction in wave speed and is a result of physical dispersion.

Direct P arrivals do not exhibit a dramatic change in arrival time or amplitude for the synthetics displayed in the bottom panel of Figure 5, but minor modifications to the compressional wave field are still noticeable at other stations. These small but detectable features are due solely to shear attenuation, Q_μ^{-1}, which is included within P wave attenuation, Q_P^{-1}. Compressional (P) wave fields, including their attenuation, involve a combination of the bulk (κ) and shear (μ) properties, in contrast to the shear (S) wave fields. The P and S inverse quality factors are, respectively,

$$Q_S^{-1} = Q_\mu^{-1}, \tag{12}$$

$$Q_P^{-1} = \left(1 - \frac{4}{3} V_S^2/V_P^2\right) Q_\kappa^{-1} + \frac{4}{3}(V_S^2/V_P^2) Q_\mu^{-1}. \tag{13}$$

Inclusion of attenuation through only Q_μ^{-1}, ignoring the effect of Q_κ^{-1}, is a reasonably safe assumption for the upper mantle on a global scale, because bulk attenuation is two orders of magnitude larger than shear attenuation (Dziewonski and Anderson, 1981). Under this assumption we have

$$Q_P^{-1} \approx \frac{4}{3}(V_S^2/V_P^2) Q_\mu^{-1}. \tag{14}$$

Subduction Zone Simulations: Seismic Arrays in Fiji and Tonga. To isolate the effects of attenuation, we computed a second set of synthetic seismograms for a selection of combined wave-speed and attenuation models. The models are either 1D or scaled versions of the 3D wave-speed model of Zhao *et al.* (1997) and attenuation model of Roth *et al.* (2000). Synthetic seismograms are compared to broadband seismic data collected from the Seismic Arrays in Fiji and

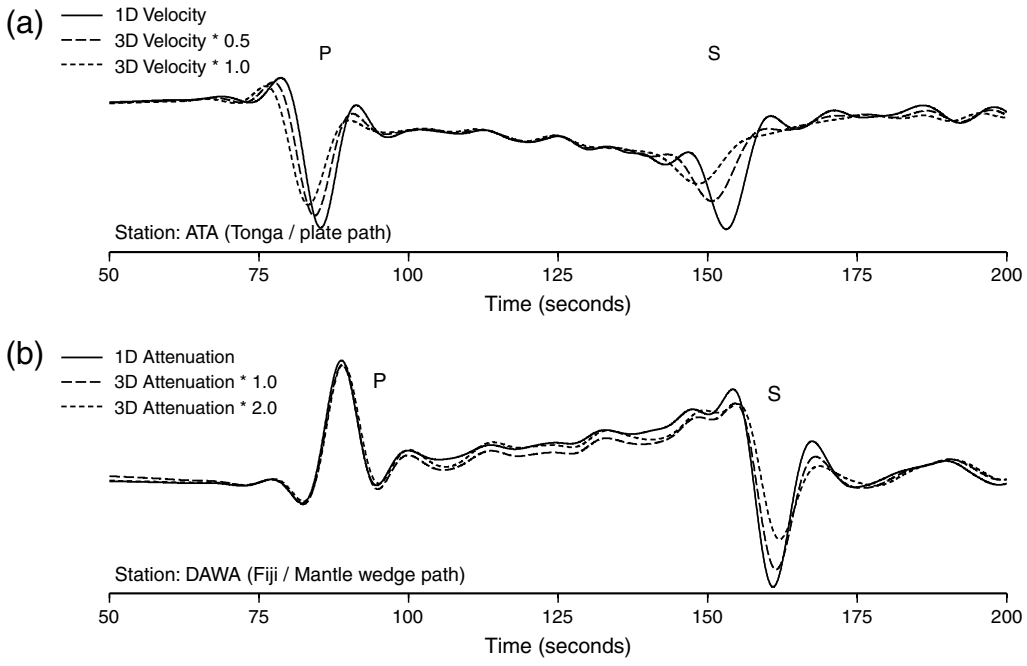

Figure 5. Vertical component synthetic seismograms for waves traveling up the slab to (a) Tonga and (b) through the mantle wedge to Fiji. (See Fig. 4 for the path geometries.) (a) The path through the fast slab results in early P and S arrivals compared with a 1D model (black). Amplitudes for the S wave are dramatically reduced, depending on the level of 3D heterogeneity (dashed and doted). Amplitudes are reduced when incorporating only wave-speed perturbations. (b) Incorporating anelastic structure in the mantle wedge demonstrates its effects on amplitude. Black seismograms are from a 1D model while dashed and dotted seismograms are from 3D models with larger magnitudes of attenuation. The direct P wave is not visibly affected by Q_μ.

Tonga (SAFT) experiment (Tibi and Wiens ,2005) from 2001 to 2002. Synthetics were computed with a minimum period of 3.3 sec for the same earthquake as in the Subduction Zone Simulations section.

Misfits of simulated phase and amplitude with respect to data for each model are displayed in Figure 6. Each data point represents a single comparison between data and synthetics. Measurements of misfit are made on the vertical component for direct *P* (Fig. 6a,c) and direct *S* arrivals (Fig. 6b,d). Phase measurements are obtained using cross correlation, while amplitude misfits are characterized through a ratio of the peak amplitudes. Seismographic stations are clustered near the islands of Tonga and Fiji in isolated azimuthal swaths traversing the mantle wedge and the subducting plate.

Measurements of phase misfit are shown in Figure 6a,b. As seen in the synthetic waveforms in the Subduction Zone Simulations section, addition of the subducting plate to a 1D wave-speed model has a profound influence on the arrival times of shear and compressional waves. Reductions of the root mean squared misfit between data and synthetics for plate

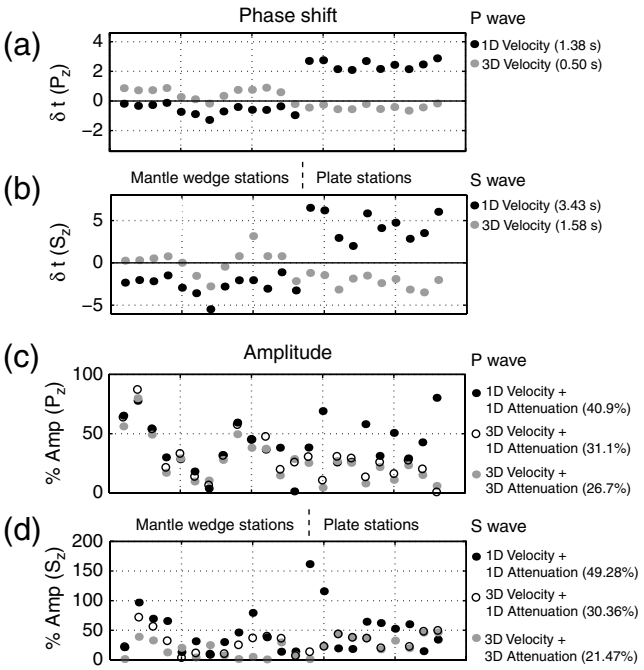

Figure 6. (a,b) Misfit of phase, and (c,d) amplitude between data and synthetics for the models in Figure 4. Direct *P* and *S* arrivals are similar to those shown in Figure 5. Differences between recorded data from the SAFT deployment and a 1D model (filled black circle), a 3D wave-speed plus 1D attenuation model (unfilled black circle), and a 3D wave-speed plus 3D attenuation model (filled gray circle) show a reduction as more heterogeneity is added. Phase misfits in (a) and (b) for the 3D wave-speed model include the 3D attenuation model. Amplitude misfit is measured as the percent error of the maximum amplitude, and phase misfit is measured in seconds; misfits are summarized to the right. While the attenuation only involves Q_μ, the *P* arrival shows improvement when the anelastic structure is applied (unfilled black circle to gray filled circle) for mantle wedge paths and for paths along the subducting plate. This is expected based upon the relation (13).

paths are about 3 sec for *P* arrivals and 5 sec for *S* arrivals. Modifications to mantle wedge wave speeds also reduce the phase misfit for mantle wedge paths. Again, the addition of anelastic structure produces negligible phase shifts at all stations, for either mantle wedge or plate paths (Fig. 5), highlighting a minimal effect of attenuation on phasing of regional arrivals. A broader and more attenuating mantle wedge structure might produce measurable phase shifts; however, this would require extremely low Q values because the current attenuation model already includes Q values ≤ 25.

Amplitude misfits are shown in Figure 6c,d. Initially, the addition of 3D wave-speed variations to a 1D model reduces the amplitude misfit between data and synthetics. Amplitude misfits for both shear and compressional wave fields are reduced regardless of the path, but much of the reduction is contained within plate paths due to the large wave-speed change associated with the subducting plate. The addition of anelastic attenuation on top of the 3D wave speed shows effects not only in the mantle wedge, but also along the plate. Much of this amplitude misfit reduction associated with attenuation is constrained to paths within the mantle wedge, which is not surprising because the anelastic attenuation is dramatic within the region. This large effect of attenuation is entirely due to the extremely low Q values, <50, within the mantle wedge. Amplitude misfit reductions associated with attenuation are present for both compressional and shear arrivals that traverse the plate. Amplitude variations due to Q_μ for *P* waves are expected (see equation 13), but the change in amplitude along the subducting plate is an unexpected result because attenuation within the plate is assumed to be reasonably small. The reduction in amplitude is likely due to increased attenuation outside of the subducting plate or to a small phase shift induced through physical dispersion.

For paths in the mantle wedge, reductions in amplitude misfit associated with attenuation are similar in magnitude to those associated with changes in wave speed. Three-dimensional models of both anelastic structure and velocity are essential to accurately replicate the amplitudes of arrivals that traverse the mantle wedge.

Global Models

At the global scale, we assess the effects of attenuation and wave speed across a wider frequency band. Our base model is transversely isotropic PREM (Dziewonski and Anderson, 1981), with 3D wave-speed variations taken from S20RTS (Ritsema *et al.*, 1999), and upper mantle Q model QRLW8 (Gung and Romanowicz, 2004), defined by 3D perturbations on top of the QL6 1D attenuation model (Durek and Ekstrom, 1996). Crustal wave speeds are included in all models through the Crust 2.0 crustal model (Bassin *et al.*, 2000). Comparisons to data are not included here because we are not evaluating the respective models and, to be shown later, an attenuation model requires an associated wave-speed model to accurately reproduce amplitudes.

Synthetic seismograms are computed for four combinations of these models: (1) our base model PREM plus 1D attenuation (M_0); (2) PREM plus QRLW8 attenuation (M_q); (3) S20RTS plus 1D attenuation (M_v); and (4) S20RTS plus QRLW8 attenuation (M_{vq}). Synthetics are computed over a period band from 27 sec to 1350 sec and for a record length of almost 4 hr, long enough to capture the third orbit of the Rayleigh wave for a single earthquake located in India.

Using the method of Ekström *et al.* (1997), amplitude and phase variations are measured from 40 sec to 250 sec at 755 broadband stations around the globe with respect to the reference model M_0. Measurements are made against a known model using a phase-matched filter to isolate the fundamental mode surface wave and suppress noise (see Ekström *et al.*, 1997 for more details). Models and ray path distributions are shown for reference in Figure 7. The measurements are plotted in Figures 8 and 9.

If 3D wave-speed variations only perturbed the phase, and attenuation only perturbed the amplitude, we could generate synthetic seismograms for each model without worry of cross-contamination. However, as in the regional simulations of the Subduction Zone Simulations section, amplitudes were substantially modified by 3D wave-speed variations as much as by 3D variations in attenuation.

Amplitude and phase perturbations relative to M_0 are plotted in Figure 8 for Rayleigh waves and Love waves for all measured periods. Amplitude perturbations due to attenuation only (M_q, top left) show a normal distribution with respect to the reference model. Measurements of amplitude ratio are expected to cluster near 1, representing an average amplitude match between the reference and the perturbed synthetics and a reasonable sampling of a wide variety of tectonic environments. Phase variations induced by the wave-speed model (M_v, bottom right) show a similar and expected behavior, but with a slight bias and nonnormal distribution due to the inclusion of higher-frequency measurements (Fig. 9) that are more susceptible to changes in wave speed. These measurements of amplitude and phase due to changes only in attenuation and wave speed, respectively, are expected.

In contrast, changes in amplitude due to only wave-speed variations (M_v, top right) and phase shifts due only to attenuation (M_q, bottom left) highlight the importance of the interaction between elastic and anelastic structures in modifying the wave field. Amplitude variations due only to wave speed (M_v, top right) show a larger range than variations due to attenuation alone (M_q, top left). This demonstrates that surface-wave amplitudes depend on wave speeds to an equal or greater extent than attenuation for this combination of wave speed and attenuation structure. Amplitude variations solely due to perturbations in wave speed are a consequence of out-of-plane focusing and defocusing arising from the interaction of the seismic wave field with lateral wave-speed variations. Amplitudes for regional arrivals in the Subduction Zone Simulations section displayed a similar dependence. Attempts to constrain attenuation without regard for wave speed will inevitably result in large artifacts and/or generally

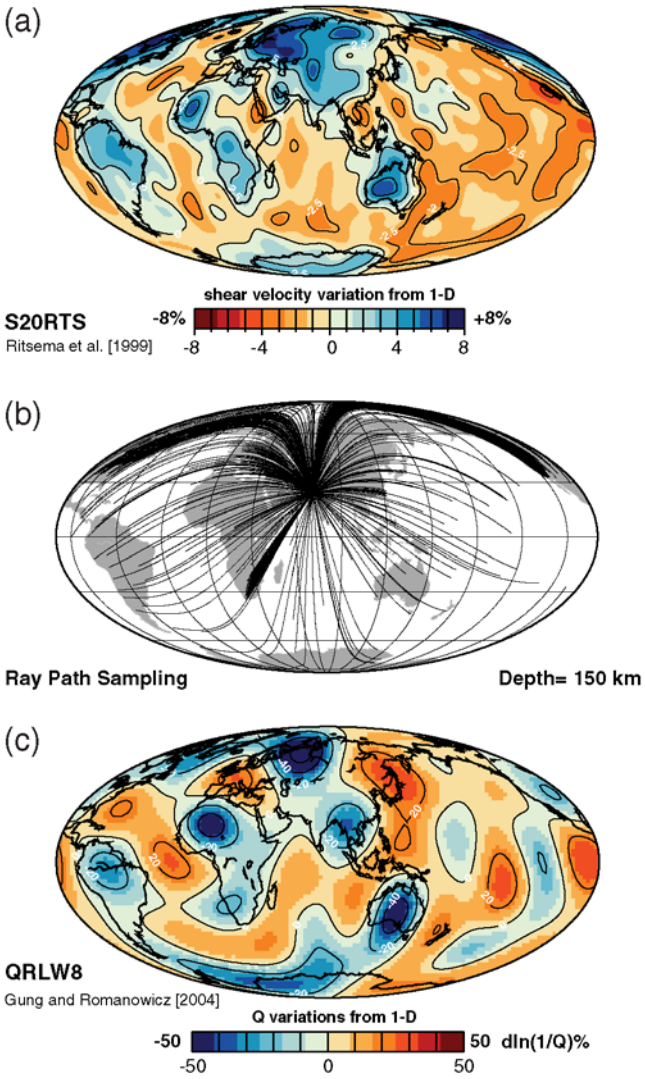

Figure 7. (a) Shear wave-speed anomalies (S20RTS, Ritsema *et al.*, 1999), (b) ray path distribution for the event in India used in the global surface wave experiment, and (c) the Q model (QRLW8, Gung and Romanowicz, 2004) used in this study. Both models are plotted at a depth of 150 km. The color version of this figure is available only in the electronic edition.

incorrect models. Further, the use of attenuation-only models to constrain global temperatures and other parameters, for example, volatiles and melt, will transfer large artifacts from seismological to geodynamical models. The strength of wave-speed-induced amplitude variations highlights the importance of starting with a good 3D wave-speed model for attenuation tomography at both regional and global scales (Romanowicz, 1994; Selby and Woodhouse, 2000; Dalton and Ekström, 2006) to account for focusing and defocusing effects (Zhou, 2009).

Changes in phase due to attenuation show much less spread than those due to wave speed, supporting the assertion that wave speeds are not dramatically affected by anelastic attenuation. Similar observations were made for the regional arrivals (Fig. 5). If an attenuation model with stronger

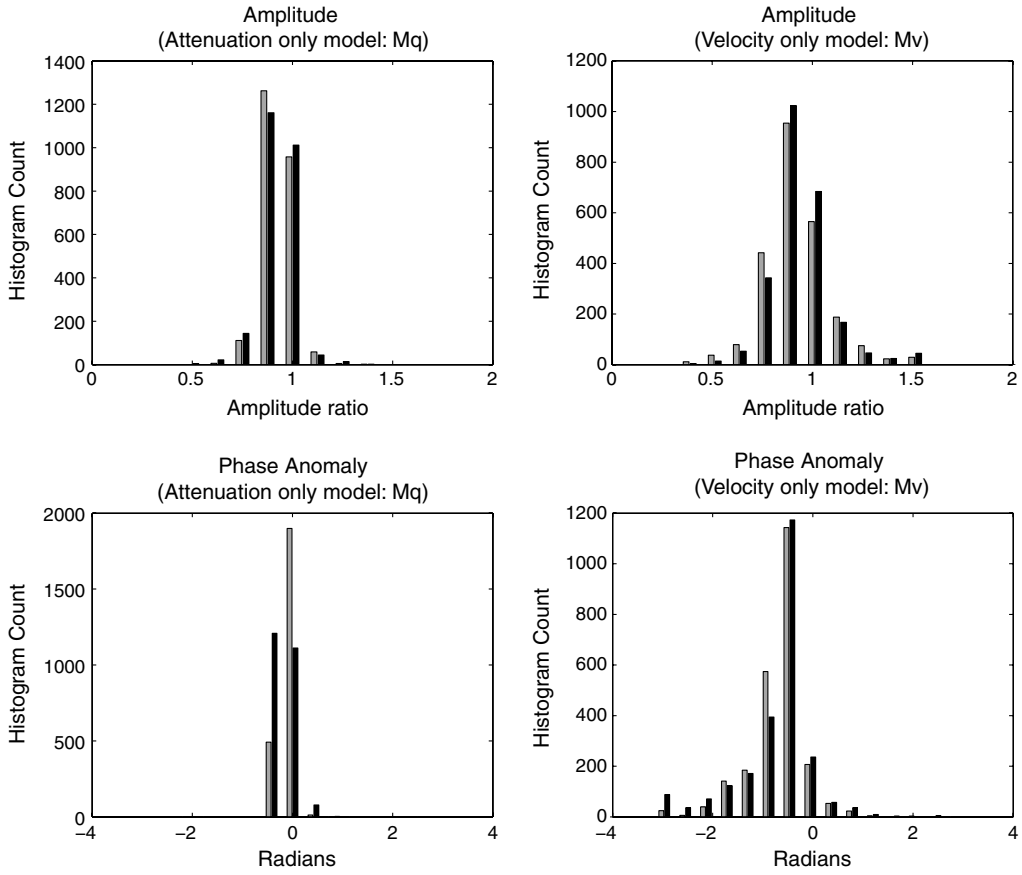

Figure 8. Misfit variations of amplitude (top) and phase (bottom) for a model with attenuation-only variations M_q (left) and a model with wave-speed-only variations M_v (right) with respect to a 1D reference model. Amplitude variations should be centered at 1 and phase variations at 0. Lateral variations in only attenuation or only wave speed, generate changes in amplitude (top left) and phase (bottom right), respectively. Moreover, amplitudes change with wave-speed variations (top right), plus phase shifts arise with the addition of anelastic structure (bottom left). Black bars denote Rayleigh waves and gray bars Love waves. Measurements of amplitude and phase are conducted using the methodology of Ekström *et al.* (1997).

contrasts were chosen (e.g., Dalton and Ekström, 2006), the phase delay results would likely indicate a stronger dependence on attenuation structure, around 15%–20% (Zhou, 2009).

Plotting measurements from global waveforms as a function of period highlights greater variations at shorter periods (Fig. 9). Amplitude perturbations due to attenuation (M_q, top left) and phase perturbations due to wave speed (M_v, bottom right) exhibit similar behavior at shorter periods for Rayleigh and Love waves. The reduction in phase is a result of lower crustal wave speeds and thicker crust near the source (Ekström *et al.*, 1997). Amplitude variations associated with wave speed (M_v, top right) show a pattern with larger amplitudes at shorter periods and somewhat smaller amplitudes at longer periods for both types of surface waves. As in Figure 8, the attenuation-induced phase variations (M_q, bottom left) do not show large perturbations at long or short periods.

Conclusions

We included 3D anelastic attenuation in the spectral-element method based upon a set of standard linear solids (SLS) and a memory-variable approach. We used this approach to illustrate the importance of attenuation in a subduction zone and on the scale of the entire globe. At regional and global scales, anelasticity plays an important role in modulating seismic amplitudes, but has a relatively minor effect on arrival times. On the other hand, wave-speed perturbations affect the phase, and produce amplitude variations with a magnitude similar to those solely due to attenuation. In general, amplitudes of seismic arrivals, either global surface waves or body waves, are due to the sometimes complex interplay between wave speed and attenuation. This has profound implications for the inference of composition, temperature, melt, or volatile content. Higher-resolution models utilizing seismic amplitude data should therefore consider effects due to attenuation and wave speed in tandem, ideally determining both in a simultaneous inversion.

Data and Resources

Seismic data from the subduction zone were collected by the Seismic Arrays in Fiji and Tonga experiment from 2001 to 2002. Simulations were carried out on a variety of

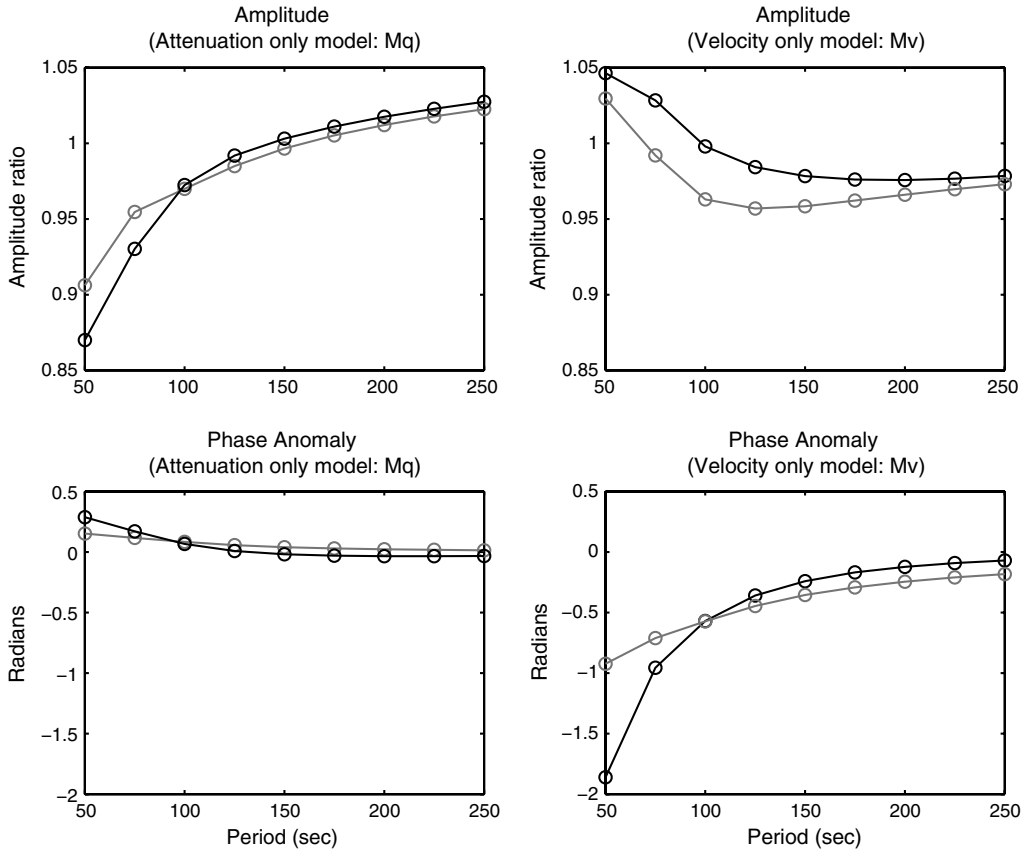

Figure 9. Mean misfits displayed against period. As in Figure 8, amplitude and phase are modified by both wave speed and attenuation. As the period of the arrival is reduced, the effect is more dramatic for both Rayleigh (black) and Love waves (gray). The offset at shorter periods is due to shorter wavelengths interacting with smaller-scale structures, causing not only a direct modification of amplitude and phase, but also bending and major distortion of the full wave field. Offsets at shorter periods are the cause of the nonnormal distributions shown in Figure 8. Data and measurements are the same as in Figure 8.

computational facilities at the San Diego Supercomputing Center (SDSC), including DataStar and the BlueGene/L machines.

Acknowledgments

Brian Savage was supported by a Carnegie Postdoctoral Fellowship during the initial stage of this work. We would like to thank Doug Wiens for information and guidance concerning the Seismic Array in Fiji and Tonga and the attenuation and wave-speed models of the Tonga–Fiji region; Yuancheng Gung and Barbara Romanowicz, as well as Jeroen Ritsema, Hendrik Jan van Heijst, and John H. Woodhouse, for providing their global models in an easy-to-use format; and Colleen Dalton for helping to make the global surface wave measurements.

References

Aki, K., and P. G. Richards (1980). *Quantitative Seismology: Theory and Methods*, W. H. Freeman, New York.

Bassin, C., G. Laske, and G. Masters (2000). The current limits of resolution for surface wave tomography in North America, *Eos Trans. AGU* **103,** 727–747.

Bhattacharyya, J., G. Masters, and P. Shearer (1996). Global lateral variations of shear wave attenuation in the upper mantle, *J. Geophys. Res.* **101,** no. B10, 22,273–22,289, doi 10.1029/96JB01782.

Boyd, O. S., C. H. Jones, and A. F. Sheehan (2004). Foundering lithosphere imaged beneath the Southern Sierra Nevada, California, USA, *Science* **305,** 660–662.

Carcione, J., D. Kosloff, and R. Kosloff (1988). Wave propagation simulation in a linear viscoelastic medium, *Geophys. J. Int.* **95,** no. 3, 597–611.

Carcione, J. M. (2007). *Wave fields in real media: Theory and numerical simulation of wave propagation in anisotropic, anelastic, porous and electromagnetic media*, Second Ed., Elsevier Science, Amsterdam, The Netherlands.

Chaljub, E., D. Komatitsch, J. Vilotte, Y. Capdeville, B. Valette, and G. Festa (2007). Spectral-element analysis in seismology, *Adv. Geophys.* **48,** 365.

Dahlen, F., and J. Tromp (1998). *Theoretical Global Seismology*, Princeton University Press, Princeton, New Jersey.

Dalton, C., and G. Ekström (2006). Global models of surface wave attenuation, *J. Geophys. Res.* **111,** no. B5, 317.

De Basabe, J., and M. Sen (2007). Grid dispersion and stability criteria of some common finite-element methods for acoustic and elastic wave equations, *Geophysics* **72,** no. T81, doi 10.1190/1.2785046.

Durek, J., and G. Ekstrom (1996). A radial model of anelasticity consistent with long-period surface-wave attenuation, *Bull. Seismol. Soc. Am.* **86,** no. 1A, 144.

Dziewonski, A., and D. Anderson (1981). Preliminary reference Earth model, *Phys. Earth. Planet. Int.* **25,** 297–356.

Ekström, G., J. Tromp, and E. Larson (1997). Measurements and global models of surface wave propagation, *J. Geophys. Res.* **102,** no. B4, 8137–8157.

Emmerich, H., and M. Korn (1987). Incorporation of attenuation into time-domain computations of seismic wave fields, *Geophysics* **52,** 1252.

Furumura, T., and B. Kennett (2008). Scattering waveguide in the heterogeneous subducting plate, in *Advances in Geophysics: Earth Heterogeneity and Scattering Effects on Seismic Waves*, H. Sato, M. Fehler (Editors), Vol. **50,** Chapter 7, Elsevier, Amsterdam, 195–217.

Gribb, T., and R. Cooper (1998). Low-frequency shear attenuation in polycrystalline olivine: Grain boundary diffusion and the physical significance of the Andrade model for viscoelastic rheology, *J. Geophys. Res.* **103,** no. B11.

Gribb, T., and R. Cooper (2000). The effect of an equilibrated melt phase on the shear creep and attenuation behavior of polycrystalline olivine, *Geophys. Res. Lett.* **27,** 15.

Gung, Y., and B. Romanowicz (2004). Q tomography of the upper mantle using three-component long-period waveforms, *Geophys. J. Int.* **157,** 813–830.

Hacker, B. R., and G. A. Abers (2004). Subduction Factory 3; an Excel worksheet and macro for calculating the densities, seismic wave speeds, and H_2O contents of minerals and rocks at pressure and temperature, *Geochem. Geophys. Geosys.* **5,** no. 1, doi 10.1029/2003GC000614.

Hammond, W., and E. Humphreys (2000a). Upper mantle seismic wave attenuation: Effects of realistic partial melt distribution, *J. Geophys. Res.* **105,** no. B5, 10,975–10,986, doi 10.1029/2000JB900041.

Hammond, W., and E. Humphreys (2000b). Upper mantle seismic wave velocity: Effects of realistic partial melt geometries, *J. Geophys. Res.* **105,** no. B5, 10,987–10,999, doi 10.1029/2000JB900042.

Jackson, I., U. Faul, J. Gerald, and B. Tan (2004). Shear wave attenuation and dispersion in melt-bearing olivine polycrystals: 1. Specimen fabrication and mechanical testing, *J. Geophys. Res.* **109,** no. B6, doi 10.1029/2003JB002406.

Kanamori, H., and D. Anderson (1977). Importance of physical dispersion in surface wave and free oscillation problems: Review, *Rev. Geophys. Space Phys* **15,** no. 105, 12.

Karato, S. (1993). Importance of anelasticity in the interpretation of seismic tomography, *Geophys. Res. Lett.* **20,** 15.

Kennett, B., and E. Engdahl (1991). Traveltimes for global earthquake location and phase identification, *Geophys. J. Int.* **105,** no. 2, 429–465.

Komatitsch, D., and J. Tromp (1999). Introduction to the spectral-element method for 3-D seismic wave propagation, *Geophys. J. Int.* **139,** 806–822.

Komatitsch, D., and J. Tromp (2002a). Spectral-element simulations of global seismic wave propagation-I. Validation, *Geophys. J. Int.* **149,** no. 2, 390–412.

Komatitsch, D., and J. Tromp (2002b). Spectral-element simulations of global seismic wave propagation-II. Three-dimensional models, oceans, rotation, and self-gravitation, *Geophys. J. Int.* **150,** 303–318.

Liu, H. P., D. L. Anderson, and H. Kanamori (1976). Velocity dispersion due to anelasticity; implications for seismology and mantle composition, *Geophys. J. R. Astr. Soc.* **47,** 41–58.

Moczo, P., and J. Kristek (2005). On the rheological models used for time-domain methods of seismic wave propagation, *Geophys. Res. Lett.* **32,** no. 1, 306, doi 10.1029/2004GL021598.

Moczo, P., J. Robertsson, and L. Eisner (2007). The finite-difference time-domain method for modeling of seismic wave propagation, in *Advances in wave propagation in heterogeneous media, Advances in Geophysics*, vol. **48,** R.-S. Wu and V. Maupin (Editors), chap. 8, pp. 421–516, Elsevier–Academic Press.

Nelder, J., and R. Mead (1965). A simplex method for function minimization, *Comput. J.* **7,** 308–313.

Nowick, A., and B. Berry (1972). *Anelastic Relaxation in Crystalline Solids*, Academic Press, New York.

Ritsema, J., H. Heijst, and J. Woodhouse (1999). Complex shear wave velocity structure imaged beneath Africa and Iceland, *Science* **286,** no. 5446, 1925.

Ritsema, J., L. Rivera, D. Komatitsch, J. Tromp, and H. van Heijst (2002). Effects of crust and mantle heterogeneity on PP/P and SS/S amplitude ratios, *Geophys. Res. Lett.* **29,** no. 10, 1430, doi 10.1029/2001GL013831.

Romanowicz, B. (1994). Anelastic tomography: A new perspective on upper mantle thermal structure, *Earth Planet. Sci. Lett.* **128,** no. 3–4, 113–121.

Roth, E. G., D. A. Wiens, L. Dorman, J. Hildebrand, and S. C. Webb (1999). Seismic attenuation tomography of the Tonga-Fiji region using phase pair methods, *J. Geophys. Res.* **104,** 4795–4809.

Roth, E. G., D. A. Wiens, and D. Zhao (2000). An empirical relationship between seismic attenuation and velocity anomalies in the upper mantle, *Geophys. Res. Lett.* **37,** no. 5, 601–604.

Selby, N. D., and J. H. Woodhouse (2000). Controls on rayleigh wave amplitudes: Attenuation and focusing, *Geophys. J. Int.* **142,** no. 3, 933–933.

Selby, N. D., and J. H. Woodhouse (2002). The Q structure of the upper mantle: Constraints from Rayleigh wave amplitudes, *J. Geophys. Res.* **107,** no. B5, 257, doi 10.1029/2001JB000.

Seriani, G., and S. Oliveira (2008). Dispersion analysis of spectral element methods for elastic wave propagation, *Wave Motion* **45,** 729–744.

Shearer, P. (1999). *Introduction to Seismology*, Cambridge University Press, New York.

Tibi, R., and D. Wiens (2005). Detailed structure and sharpness of upper mantle discontinuities in the Tonga subduction zone from regional broadband arrays, *J. Geophys. Res.* **110,** no. B6, B06313.

Warren, L. M., and P. M. Shearer (2000). Investigating the frequency dependence of mantle Q by stacking P and PP spectra, *J. Geophys. Res.* **105,** no. B11.

Warren, L. M., and P. M. Shearer (2002). Mapping lateral variation in upper mantle attenuation by stacking P and PP spectra, *J. Geophys. Res.* **107,** no. B12, doi 10.1029/2001JB001195.

Widmer, R., G. Masters, and F. Gilbert (1991). Spherically symmetric attenuation within the Earth from normal mode data, *Geophys. J. Int.* **104,** 541–553.

Wiens, D. A., and G. P. Smith (2003). Seismological constraints on structure and flow patterns within the mantle wedge, in *Inside the Subduction Factory*, J. Eiler (Editor), **138,** pp. 59–82, AGU Monograph.

Zhao, D., Y. Xu, D. A. Wiens, L. Dorman, J. Hildebrand, and S. Webb (1997). Depth extend of the Lau back-arc spreading center and its relation to subduction processes, *Science* **278,** 254–257.

Zhou, Y. (2009). Surface-wave sensitivity to 3-D anelasticity, *Geophys. J. Int.* **178,** no. 3, 1403–1410.

University of Rhode Island
9 East Alumni Avenue, 317 Woodward Hall
Kingston, Rhode Island 02881
savage@uri.edu
(B.S.)

Université de Pau et des Pays de l'Adour
CNRS & INRIA Magique-3D
Laboratoire de Modélisation et d'Imagerie en Géosciences UMR 5212
Avenue de l'Université
64013 Pau Cedex, France
(D.K.)

Princeton University
Guyot Hall, Princeton
New Jersey 08544
(J.T.)

Manuscript received 27 August 2009